nature communications

Article

https://doi.org/10.1038/s41467-024-51873-x

IL36G-producing neutrophil-like monocytes promote cachexia in cancer

Received: 24 September 2023

Accepted: 19 August 2024

Published online: 12 September 2024

Check for updates

Yoshihiro Hayashi[1,2,4] ✉, Yasushige Kamimura-Aoyagi[1,4], Sayuri Nishikawa[1], Rena Noka[1], Rika Iwata[1], Asami Iwabuchi[1], Yushin Watanabe[1], Natsumi Matsunuma[1], Kanako Yuki[1], Hiroki Kobayashi[1], Yuka Harada[3] & Hironori Harada[1] ✉

Most patients with advanced cancer develop cachexia, a multifactorial syndrome characterized by progressive skeletal muscle wasting. Despite its catastrophic impact on survival, the critical mediators responsible for cancer cachexia development remain poorly defined. Here, we show that a distinct subset of neutrophil-like monocytes, which we term cachexia-inducible monocytes (CiMs), emerges in the advanced cancer milieu and promotes skeletal muscle loss. Unbiased transcriptome analysis reveals that interleukin 36 gamma (IL36G)-producing CD38$^+$ CiMs are induced in chronic monocytic blood cancer characterized by prominent cachexia. Notably, the emergence of CiMs and the activation of CiM-related gene signatures in monocytes are confirmed in various advanced solid cancers. Stimuli of toll-like receptor 4 signaling are responsible for the induction of CiMs. Genetic inhibition of IL36G-mediated signaling attenuates skeletal muscle loss and rescues cachexia phenotypes in advanced cancer models. These findings indicate that the IL36G-producing subset of neutrophil-like monocytes could be a potential therapeutic target in cancer cachexia.

Cachexia comprises a group of multifactorial inflammatory and metabolic syndromes defined by progressive weight loss and skeletal muscle wasting independent of whether fat mass loss occurs[1,2]. Cancer-associated cachexia is often observed in patients with various cancers, particularly in advanced stages, with a prevalence of approximately 80%[1]. However, the mechanisms underlying cachexia development in cancer pathogenesis remain unclear. Although cachexia is estimated to account for up to 30% of all cancer-related deaths[3], limited therapeutic options are currently available.

Recent advances in cancer biology have uncovered critical pro- and anti-tumor roles of immune cells in the generation and progression of cancer pathogenesis[4–6]. Among these immune cells, myeloid innate immune cells, including neutrophils, monocytes, macrophages, and dendritic cells, are key components of the complex cancer-associated ecosystem[7–15]. Accumulating evidence demonstrates that cancer cells can reprogram these immune cells toward a tumor-promoting phenotype, not only within the tumor microenvironment (TME) but also in systemic circulation. This can facilitate tumor growth, invasion, metastasis, immune escape, and therapy resistance, leading to disease progression and dismal outcomes in patients with cancer[14,16]. Given that cachexia primarily occurs in advanced cancer[1], tumor-educated myeloid innate immune cells likely contribute to the pathogenesis of cancer cachexia. Indeed, increased expression of several cytokines and chemokines, such as tumor necrosis factor (TNF), interleukin 1 (IL1), and IL6, has been reported in patients with cancer cachexia[17]. Besides tumor cells, many myeloid innate immune cells are capable of producing these proinflammatory factors[18]. C-C motif chemokine ligand (CCL2), a master chemoattractant for

[1]Laboratory of Oncology, School of Life Sciences, Tokyo University of Pharmacy and Life Sciences, Tokyo, Japan. [2]Laboratory of Cancer Pathobiology and Therapeutics, College of Pharmaceutical Sciences, Ritsumeikan University, Shiga, Japan. [3]Clinical Research Support Center, Tokyo Metropolitan Cancer and Infectious Diseases Center, Komagome Hospital, Tokyo, Japan. [4]These authors contributed equally: Yoshihiro Hayashi, Yasushige Kamimura-Aoyagi. ✉e-mail: yshrhys@fc.ritsumei.ac.jp; hharada@toyaku.ac.jp

monocytes, also exhibits high expression levels in serum from patients with cancer, particularly those with cachexia[19]. Several reports also demonstrated the relevance of neutrophils in cachexia[20,21]. However, the subset of myeloid innate immune cells that play a central role in cancer cachexia development remains unclear.

An increase in circulating monocytes is often associated with a poor prognosis in patients with both blood and solid cancers[22–25]. In blood cancers, an absolute increase in peripheral blood (PB) classical monocytes is a characteristic clinical feature of chronic myelomonocytic leukemia (CMML), a hematopoietic clonal disorder characterized by persistent monocytosis. In addition to the hematological phenotype, systemic symptoms such as fatigue, weight loss, and cachexia are common clinical features of patients with CMML[26,27]. These systemic symptoms are prominent in patients with CMML, suggesting that a subpopulation of classical monocytes could be responsible for these phenomena.

Here, we identify a distinct subset of inflammatory monocytes that exhibits neutrophil-like characteristics and facilitates progressive skeletal muscle atrophy in a discrete type of blood cancer pathogenesis. Importantly, we find that these monocytes are also prominently induced in the context of solid cancer-derived cachexia and that inhibition of this monocyte-derived inflammatory axis could blunt the development of cachexia.

Results

Cachexia development in monocytic leukemia mice

To investigate the mechanisms of cachexia development in blood cancer with monocytosis, we used a monocytic leukemia (Mo-Leukemia) mouse model that was established using a CMML patient-derived *NUP98-HBO1* mutant[28]. The characteristic monocytosis seen in CMML is induced in this model[28]. We retrovirally introduced the *NUP98-HBO1* mutant into wild-type (WT) murine hematopoietic stem cells and progenitors (HSC/Ps) and transplanted them into WT recipient mice (Mo-Leukemia mice) (Fig. 1a). Mice transplanted with empty vector-transduced cells served as the controls. Persistent monocytosis and an increase in the subset of $CD14^+$ $CD16^-$ classical monocytes are hallmarks of CMML that separate it from other monocytic disorders with high sensitivity and specificity[26]. Consistent with these clinical findings, the Mo-Leukemia mice exhibited prominent monocytosis (Fig. 1b–d). The subset of $CD115^+$ $Ly6C^{high}$ monocytes, an equivalent subpopulation of human classical monocytes, was significantly increased in PB from Mo-Leukemia mice (Fig. 1e). The frequency of bone marrow (BM) monocytes was also higher in Mo-Leukemia mice than in control mice (Fig. 1f). In addition to the hematological phenotypes, the Mo-Leukemia mice showed progressive weight loss (Fig. 1g). Skeletal muscle weight and fiber cross-sectional area (CSA) were significantly lower in Mo-Leukemia mice with weight loss than in control mice (Fig. 1h–j and Supplementary Fig. 1). Furthermore, genes related to skeletal muscle atrophy, such as *Trim63* and *Fbxo32* (also known as *MuRF1* and *Atrogin1*, respectively)[1], were prominently upregulated in the skeletal muscle (quadriceps) of Mo-Leukemia mice with weight loss compared to those in control mice (Fig. 1k). Mo-Leukemia mice with weight loss exhibited lower grip strength than control mice (Fig. 1l). These results suggest that Mo-Leukemia mice develop cancer cachexia, characterized by skeletal muscle wasting and weakness.

Considering that persistent characteristic monocytosis and cachexia development are characteristic clinical features of CMML, it is likely that the subpopulation of classical monocytes is responsible for the development of cachexia. To test this hypothesis, we collected BM $CD115^+$ $Ly6C^{high}$ monocytes from Mo-Leukemia or control mice and cultured them with differentiated murine C2C12 myotubes in a transwell system (Fig. 1m and Supplementary Fig. 2). We observed a significant decrease in the diameter of C2C12 myotubes upon co-culture with $CD115^+$ $Ly6C^{high}$ inflammatory monocytes from Mo-Leukemia mice (Fig. 1n, o). In contrast, $Ly6G^+$ granulocytes from Mo-Leukemia mice did not affect the diameter of C2C12 myotubes (Fig. 1o). These results indicate that the inflammatory monocytes from cachectic Mo-Leukemia mice contain cachexia-inducible monocytes that could be termed cachexia-inducible monocytes (CiMs).

IL36G-expressing $CD38^+$ CiMs induce muscle atrophy

To characterize the gene expression profile of inflammatory monocytes in Mo-Leukemia mice with cachexia, we performed bulk RNA sequencing (RNA-seq) of BM $CD115^+$ $Ly6C^{high}$ inflammatory monocytes obtained from Mo-Leukemia mice, with or without weight loss, and control mice (Fig. 2a). Principal component analysis revealed a unique gene expression pattern in inflammatory monocytes derived from Mo-Leukemia mice with cachexia (Fig. 2b). Many genes were upregulated in Mo-Leukemia monocytes compared with control monocytes (Fig. 2c and Supplementary Data 1). We re-clustered these genes and identified gene clusters (clusters 7 and 8) that were upregulated in Mo-Leukemia mice with cachexia compared to those without weight loss (Fig. 2d and Supplementary Data 2). Genes in cluster 7, in particular, were enriched in Gene Ontology (GO); biological processes related to granulocyte and neutrophil activation (Fig. 2d). Given that inflammatory monocytes from cachectic Mo-Leukemia mice induced skeletal muscle atrophy even in an indirect co-culture setting (Fig. 1m–o), we hypothesized that these monocytes might produce signaling molecules that could promote skeletal muscle wasting. To identify cachexia-inducible molecules derived from monocytes, we intersected genes in clusters 7/8 with a GO-term related to receptor ligand activity (GO:0048018) (Fig. 2e). Among the six genes identified using intersection analysis, *Il36g* (also known as *Il1f9*) comprised the significantly expressed genes in the inflammatory monocytes from cachectic Mo-Leukemia mice (but not mice without weight loss) (Fig. 2f).

Characteristic cell surface molecules enable the isolation of specific cell subsets within a heterogeneous cell population using immunological techniques, including flow cytometry and fluorescence microscopy. To identify surface markers that discriminate CiMs from other monocytes, we also intersected genes in clusters 7/8 from the bulk RNA-Seq analysis (Fig. 2d) with a GO-term related to the plasma membrane (GO:0005886) (Fig. 2g). Among the genes upregulated in $CD115^+$ $Ly6C^{high}$ inflammatory monocytes from cachectic Mo-Leukemia mice, *Cd38* was the most significantly expressed (Fig. 2h and Supplementary Data 3). We confirmed protein expression using flow cytometry and found that CD38 protein was prominently expressed in PB $CD115^+$ $Ly6C^{high}$ inflammatory monocytes from cachectic Mo-Leukemia mice compared with those from control or non-cachectic mice (Fig. 2i, j). These $CD38^+$ $CD115^+$ $Ly6C^{high}$ inflammatory monocytes exhibited monocyte/macrophage morphology (Fig. 2k). CD38 expression was also detected in BM $CD115^+$ $Ly6C^{high}$ inflammatory monocytes from cachectic Mo-Leukemia mice (but not Mo-Leukemia mice without weight loss) (Fig. 2l). Furthermore, the diameter of C2C12 myotubes significantly decreased upon co-culture with $CD38^+$ $CD115^+$ $Ly6C^{high}$ inflammatory monocytes from cachectic Mo-Leukemia mice compared to $CD115^+$ $Ly6C^{high}$ inflammatory monocytes from control mice or $CD38^-$ $CD115^+$ $Ly6C^{high}$ inflammatory monocytes from cachectic Mo-Leukemia mice (Fig. 2m). The expression levels of *Trim63* and *Fbxo32* mRNA were also increased in C2C12 myotubes upon co-culture with $CD38^+$ $CD115^+$ $Ly6C^{high}$ inflammatory monocytes from Mo-Leukemia mice (Supplementary Fig. 3). We confirmed *Il36g* mRNA expression and Il36g protein production in the $CD38^+$ inflammatory monocytes (Fig. 2n–p). Taken together, these results suggest that the Il36g-producing subset of inflammatory monocytes can function as "CiMs" and promote cachexia development in Mo-Leukemia mice. CD38 could serve as a useful surface marker for IL36G-producing CiMs.

Neutrophil-like gene signature in IL36G-producing CiMs

To confirm that induction of CiMs is not a consequence of the progression of severe cachexia, we isolated $CD115^+$ $Ly6C^{high}$ BM

https://doi.org/10.1038/s41467-024-51873-x

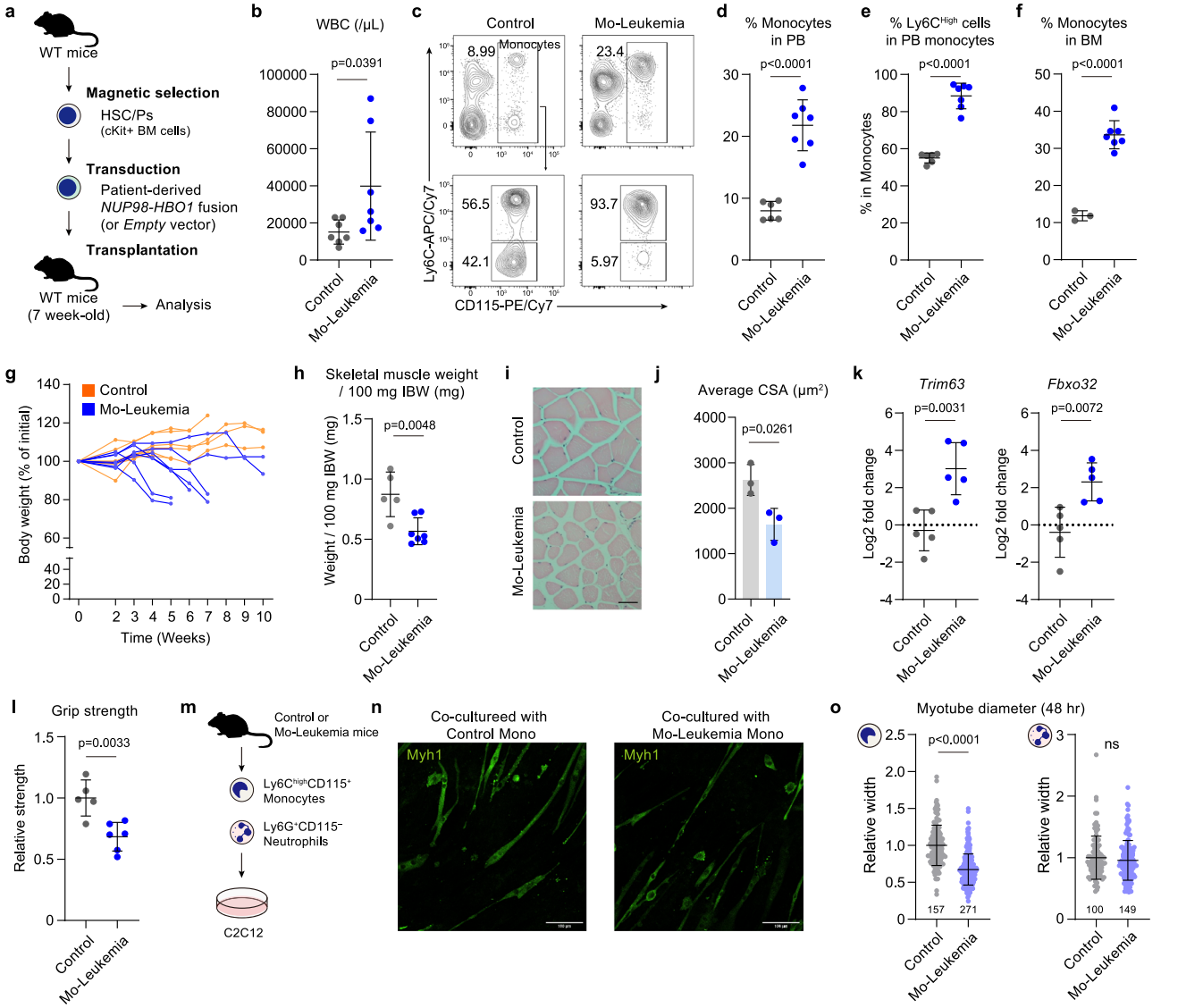

Fig. 1 | Cachexia development in monocytic leukemia mice. a Schematic of experimental design. **b** White blood cell (WBC) counts in PB from control and Mo-Leukemia mice ($n = 7$ mice per each). **c**–**e** Flow cytometric analysis of total PB from control ($n = 6$ mice) and Mo-Leukemia mice ($n = 7$ mice). Representative flow cytometry plots (**c**), frequencies of total monocytes in PB (**d**) and Ly6C$^+$ inflammatory monocytes in total monocytes (**e**) are shown. **f** Flow cytometric analysis of total BM cells from control ($n = 3$ mice) and Mo-Leukemia ($n = 7$ mice) mice. The frequencies of monocytes in BM are shown. **g** Body weight of the control and Mo-Leukemia mice ($n = 7$ mice per group) after transplantation. **h** Skeletal muscle weights of control ($n = 5$ mice, at 6 to 10 weeks after BMT) and Mo-Leukemia mice ($n = 7$ mice, at the endpoint or 10 weeks after BMT). Weights are normalized to the initial body weight (IBW) and presented as weight/100 mg IBW. **i**, **j** HE staining and cross-sectional area (CSA) of quadriceps from control and Mo-Leukemia mice ($n = 3$ mice per group). Representative images (**i**) and average (**j**) of CSA are shown. Scale bar, 50 μm. **k** mRNA expression levels of muscle atrophy markers in quadriceps from control and Mo-Leukemia mice ($n = 5$ mice per each) at the endpoint. Log2 fold change values compared to mean values of control are shown. **l** Forelimb grip strength of control ($n = 5$) and Mo-Leukemia mice ($n = 6$ mice) at the endpoint. The values were normalized to those of the control group. **m** Schematic of the co-culture assay. **n** Representative immunofluorescence images of C2C12 myotubes. Scale bar, 100 μm. **o** Relative diameter of C2C12 myotubes after co-culture with inflammatory monocytes and neutrophils. Representative results from more than three independent experiments are shown. The number of muscle fibers analyzed in each sample is shown. Statistical analyses were performed using a two-tailed unpaired Student's *t*-test. Data are presented as the mean ± SD. NS is not significant. Source data are provided as a Source Data file.

inflammatory monocytes from Mo-Leukemia mice at the time of pre-cachexia, when weight loss began to appear, and performed single-cell RNA-Seq (scRNA-Seq) analysis (Fig. 3a). We then compared the results with those of control mice using the Cellranger aggr pipeline and identified 10 clusters based on t-distributed stochastic neighbor embedding (t-SNE) plots (Fig. 3b). Among these clusters, clusters 2, 7, and 8 were primarily composed of inflammatory monocytes from the Mo-Leukemia mice (Fig. 3b). Pathway enrichment analysis showed that the distinctively upregulated genes in these three clusters were enriched for several signaling pathways related to neutrophil regulation and inflammation (Fig. 3c and Supplementary Data 4). Notably, cells expressing *Il36g* were primarily included in these clusters (Fig. 3d). Some of *Il36g*-expressing cells were also included in clusters 1 and 3 (Fig. 3b, d and Supplementary Data 4). To further characterize the gene signature of cells expressing *Il36g* at the time of pre-cachexia, we processed the scRNA-Seq data of inflammatory monocytes from Mo-Leukemia mice using iterative clustering and guide-gene selection (ICGS) algorithm, an unsupervised discovery workflow that can resolve rare and transitional populations in scRNA-Seq datasets[29]. ICGS resolved nine clusters and revealed a unique cluster (cluster #4) in which *Il36g*-expressing CiMs were significantly enriched (Fig. 3e–g and Supplementary Data 5). We note that many granulocyte-related genes,

https://doi.org/10.1038/s41467-024-51873-x

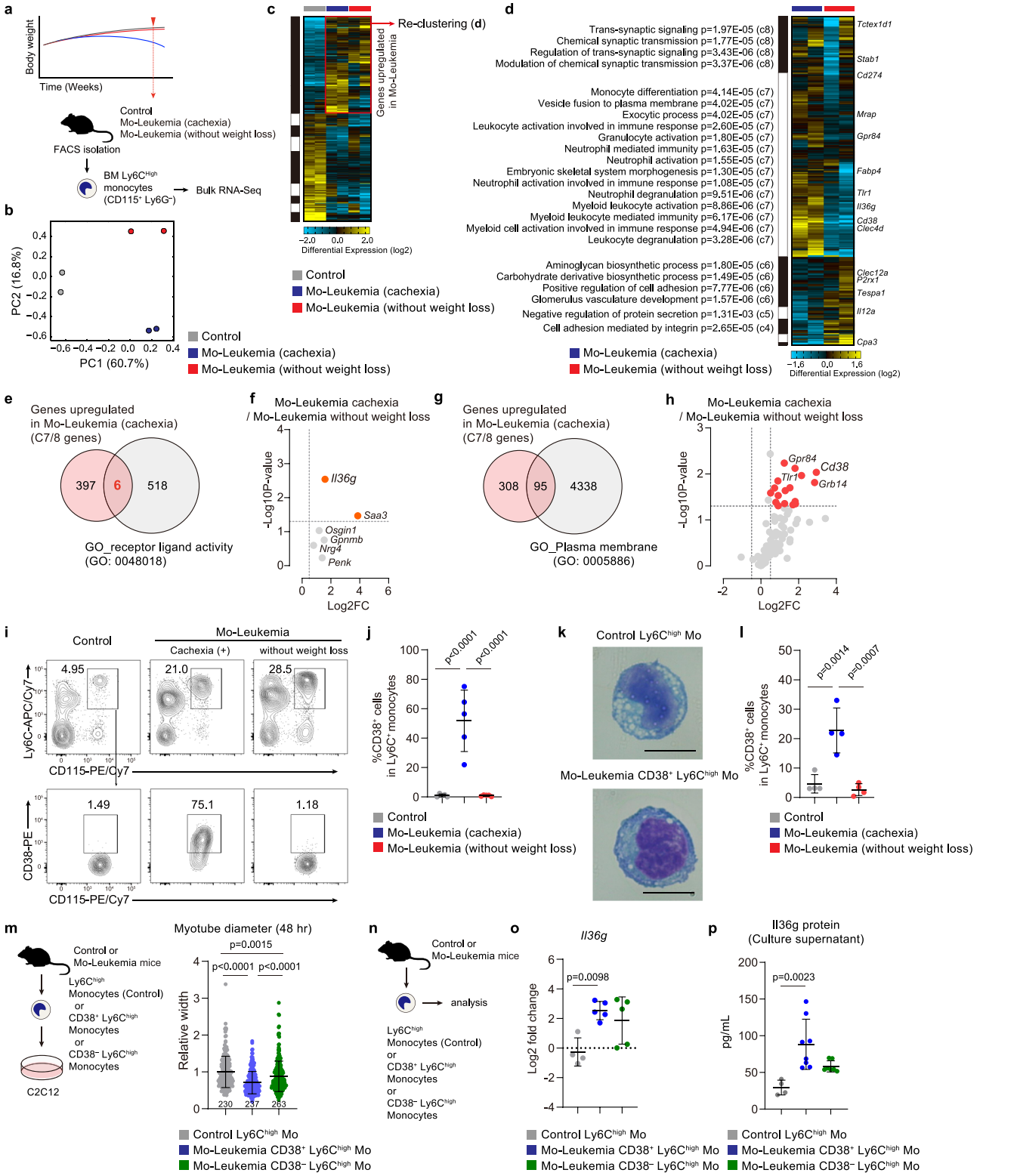

such as *Prtn3*, *Ctsg*, *Elane*, *S100a8*, *S100a9*, and *Cebpe*, were highly expressed in this CiM-enriched cluster (Fig. 3e). The upregulated differentially expressed genes (DEGs) in *Il36g*-expressing CiMs in comparison to cells without *Il36g* expression (non-CiMs) included many neutrophil-related genes (Fig. 3h). GO-term enrichment analysis showed that these upregulated DEGs in CiMs were significantly enriched for neutrophil regulation and activation (Fig. 3i and Supplementary Data 6). Taken together, these results suggest that IL36G-producing CiMs exhibit neutrophil-like characteristics.

Yáñez et al. demonstrated that neutrophil-like inflammatory monocytes differentiate from granulocyte-monocyte progenitors (GMPs) upon toll-like receptor 4 (TLR4) stimulation[30]. Given that the CiMs exhibited a neutrophil-like gene signature, they likely belong to the subtype of neutrophil-like monocytes and could, therefore, be induced in response to TLR4 stimuli. To test this hypothesis, we injected lipopolysaccharide (LPS), a TLR4 agonist[31,32], into both non-cachectic Mo-Leukemia mice and WT control mice. As expected, we observed the emergence of the *Il36g*-expressing CD38^{+} CD115^{+} Ly6C^{high}

Fig. 2 | Identification of IL36G-producing CiMs. a Schematic of sample collection for bulk RNA-Seq ($n = 2$ independent samples per each). **b** Principal component analysis for bulk RNA-seq data of BM CD115$^+$ Ly6C^{high} inflammatory monocytes obtained from the indicated mice. **c** HOPACH-generated clusters of differentially expressed genes in CD115$^+$ Ly6C^{high} inflammatory monocytes from the indicated mice. **d** Heat map of re-clustered genes upregulated in Mo-Leukemia mice (HOPACH algorithm) with statistically enriched Gene Ontology (GO) terms (left) and enriched GO term-associated genes (right). The upregulated genes in Mo-Leukemia mice (**c**) were re-clustered. **e**, **f** Receptor-ligand-related genes in DEGs upregulated in CD115$^+$ Ly6C^{high} inflammatory monocytes from cachectic Mo-Leukemia mice (**e**). For the six selected genes, volcano plots in the indicated comparisons are shown in (**f**). **g**, **h** Plasma membrane-related genes among DEGs upregulated in CD115$^+$ Ly6C^{high} inflammatory monocytes from cachectic Mo-Leukemia mice (**g**). For the selected 95 genes, a volcano plot in the indicated comparison is shown in (**h**). **i**, **j** Flow cytometric analysis of total PB from the control, Mo-Leukemia mice with cachexia, and Mo-Leukemia mice without weight loss ($n = 5$ mice per group). Representative flow cytometry plots (**i**) and the frequencies of CD38$^+$ cells in PB Ly6C$^+$ inflammatory monocytes (**j**) are shown. **k** Diff-Quik staining of CD38$^+$ Ly6C$^+$ inflammatory monocytes from Mo-Leukemia mice with cachexia. Scale bar, 10 μm. **l** Flow cytometric analysis of the total BM from control, Mo-Leukemia mice with cachexia, and Mo-Leukemia mice without weight loss ($n = 4$ mice per each). The frequencies of CD38$^+$ cells in BM Ly6C$^+$ inflammatory monocytes are shown. **m** Relative diameters of C2C12 myotubes after the co-culture assay with the indicated cells. Representative results from more than three independent experiments are shown. The number of muscle fibers analyzed in each sample is shown. **n** Schematic of sample collection. **o** mRNA expression levels of *Il36g* in control Ly6C$^+$ monocytes ($n = 4$ mice), CD38$^+$ Ly6C$^+$ inflammatory monocytes from Mo-Leukemia mice ($n = 5$ mice), and CD38$^-$ Ly6C$^+$ inflammatory monocytes from Mo-Leukemia mice ($n = 5$ mice). **p** Expression level of Il36g protein in the culture supernatant of control Ly6C$^+$ monocytes ($n = 4$ mice), CD38$^+$ Ly6C$^+$ inflammatory monocytes from Mo-Leukemia mice ($n = 5$ mice), and CD38$^-$ Ly6C$^+$ inflammatory monocytes from Mo-Leukemia mice ($n = 5$ mice). Statistical analyses were performed using Fisher's exact test (**d**), empirical Bayes moderated *t* test (**f**, **h**), and one-way ANOVA followed by Tukey multiple comparison test (**j**, **l**, **m**, **o**, **p**). Data are presented as the mean ± SD (**j**, **l**, **m**, **o**, **p**). Source data are provided as a Source Data file.

inflammatory monocytes in Mo-Leukemia mice (Supplementary Fig. 4a, b). In contrast, administration of unmethylated CpG DNA, an agonist of TLR9 that could promote inflammatory monocyte differentiation from monocyte-dendritic cell progenitors (MDPs)[30], did not induce CD38$^+$ CD115$^+$ Ly6C^{high} inflammatory monocytes in Mo-Leukemia mice (Supplementary Fig. 4a). Furthermore, we tested the upregulated DEGs in CiMs in bulk RNA-Seq dataset of GMP- and MDP-derived inflammatory monocytes (GSE88982)[30] using gene set enrichment analysis (GSEA) and found that these genes were significantly enriched in GMP-derived neutrophil-like monocytes (Supplementary Fig. 4c). Interestingly, some of the neutrophil-related genes, such as *Ctsg*, *Elane*, *Mpo*, and *Prtn3*, were not upregulated in CD38$^+$ CD115$^+$ Ly6C^{high} inflammatory monocytes in Mo-Leukemia mice after LPS administration. These results suggest the heterogeneity of neutrophil-like monocytes and the existence of a unique subset of neutrophil-like monocytes in the context of cancer pathogenesis.

Emergence of CiMs in solid-tumor mediated cancer cachexia

A significant association between an increase in circulating monocytes and a poor prognosis has been reported in both blood and solid cancers[22–25]. Given that cancer cachexia is primarily observed in patients with advanced stages of cancer, we hypothesized that CiMs might also be involved in the pathogenesis of cachexia in solid cancers. To test this hypothesis and evaluate the tumor-related immune cell dynamics, we generated solid tumor-bearing syngeneic models using 4T1 cells (metastatic murine breast cancer cells) and B16 cells (murine melanoma cells), both of which are established models of cancer cachexia[33–37]. By intravenously injecting 4T1 breast cancer cells and B16 melanoma cells, we generated mouse models of systemic hematogenous metastasis (Fig. 4a). As expected, cachexia with skeletal muscle atrophy and weakness was observed in all of these mice with systemic hematogenous metastasis (Fig. 4b–g, Supplementary Fig. 5 and Supplementary 6a–e). This is consistent with previous reports of the link between systemic metastasis and cancer cachexia development[23]. Flow cytometric analysis revealed that the frequency of CD38$^+$ CD115$^+$ Ly6C^{high} inflammatory monocytes prominently increased in both PB and BM from these cachectic 4T1 and B16 metastasis models (Fig. 4h–j and Supplementary Fig. 6f, g). Morphological features of these monocytes were confirmed (Fig. 4k). Furthermore, these CD38$^+$ CD115$^+$ Ly6C^{high} inflammatory monocytes induced a significant decrease in the diameter of C2C12 myotubes in the transwell indirect co-culture system (Fig. 4l), suggesting that CiMs are induced in the pathogenesis of solid tumor-mediated cancer cachexia. Consistent with the observation in the blood cancer model, we also confirmed the upregulation of mRNA expression levels of *Il36g* and neutrophil-related genes in CD38$^+$ CD115$^+$ Ly6C^{high} inflammatory monocytes isolated from cachectic solid tumor models (Fig. 4m, n and Supplementary Fig. 6h, i). To confirm the TLR4 stimuli-mediated induction of CiMs in the advanced solid cancer pathogenesis, we pharmacologically inhibited TLR4 in the 4T1 and B16 metastasis models using TAK-242, a specific inhibitor of TLR4 signaling[38] (Fig. 4o and Supplementary Fig. 6j). The induction of CD38$^+$ CiMs was significantly suppressed in the TAK242-treated metastasis models compared with that in the vehicle controls (Fig. 4o–q and Supplementary Fig. 6k, l), suggesting that TLR4 signaling activation is responsible for CiM induction in cancer pathogenesis. These results suggest that CiMs are induced in the pathogenesis of solid tumor-mediated cancer cachexia.

To further validate CiM emergence in the context of advanced solid tumor-mediated cancer cachexia, we analyzed a dataset of inflammatory monocytes obtained from mice with breast cancer bone metastasis (GSE152795)[39]. Neutrophil-related genes, including *Il36g* and *Cd38*, were significantly upregulated in inflammatory monocytes from mice with advanced breast cancer compared to those from control mice (Supplementary Fig. 7a, b). The upregulated DEGs in CiMs were significantly enriched in the inflammatory monocytes from mice with advanced breast cancer (Supplementary Fig. 7c). We also tested the upregulated DEGs in CiMs in the human datasets of classical monocytes obtained from patients with colorectal cancer (CRC) and renal cell carcinoma (RCC), in which cachexia is commonly observed (GSE47756 and GSE38424)[40,41]. The CRC cohort included patients with non-metastatic CRC ($n = 27$), patients with metastatic CRC ($n = 28$), and healthy donors ($n = 38$). The RCC cohort included patients with RCC ($n = 4$) and healthy donors ($n = 4$). Consistent with the findings in multiple mouse models of cancer cachexia, the upregulated DEGs in CiMs were significantly enriched in the classical monocytes of patients with CRC (particularly in the metastatic CRC group) and RCC (Supplementary Fig. 8a, b). Notably, the upregulated DEGs in CiMs were particularly enriched in the metastatic CRC cohort compared with the non-metastatic CRC cohort (Supplementary Fig. 8a). This is consistent with the fact that cachexia occurs primarily in advanced cancer with invasion and metastasis. These results suggest that the emergence of neutrophil-like CiMs is a common pathobiological phenomenon in cancer cachexia.

Targeting IL36G signaling in cancer cachexia

Our data obtained from mouse models of blood and solid cancers indicate that the IL36G-mediated signaling pathway is responsible for cancer cachexia development. To investigate the clinical relevance of IL36G levels in patients with cancer cachexia, we measured IL36G levels in the serum of patients with advanced cancer with cachexia in the palliative care unit (Supplementary Data 7). Among the advanced cancer patients who met the diagnosis criteria for cachexia, seven out

https://doi.org/10.1038/s41467-024-51873-x

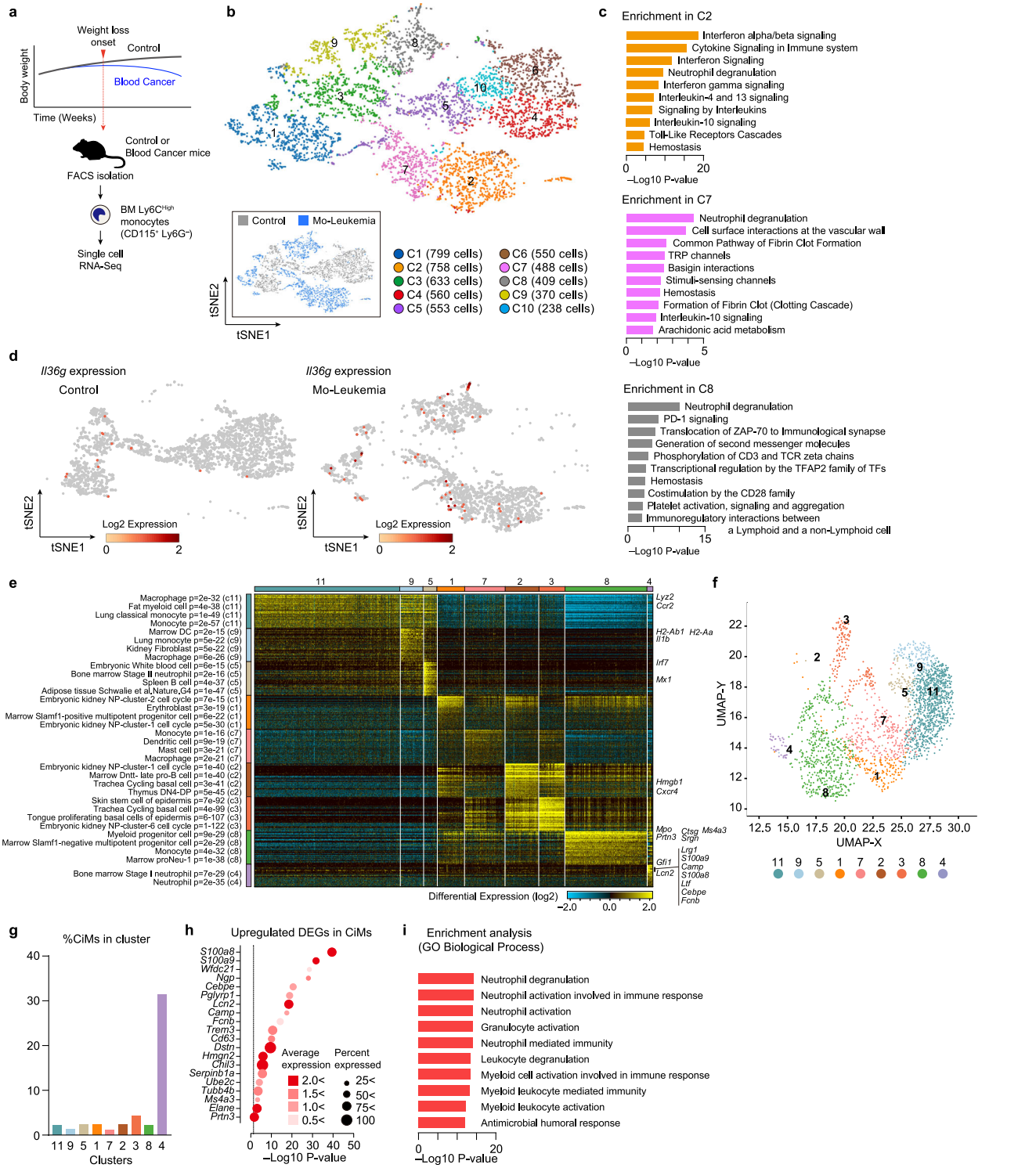

Fig. 3 | CiMs exhibit neutrophil-like gene signature. a Schematic of sample collection for scRNA-Seq. **b** t-SNE plot of 5358 single cells distributed using a graph-based clustering algorithm (Cell Ranger). **c** Pathway enrichment analysis for differentially expressed genes in indicated clusters. **d** Expression intensity and distribution of *Il36g* are overlaid on the tSNE plot. **e**, **f** Heat map and uniform manifold approximation and projection (UMAP) of genes delineated by ICGS in scRNA-seq data of inflammatory monocytes from Mo-Leukemia mice at the time of cachexia onset. **g** Frequency of *Il36g*-expressing CiMs in individual ICGS clusters. **h** DEGs upregulated in *Il36g*-expressing CiMs. **i** GO-term enrichment analysis of DEGs upregulated in *Il36g*-expressing CiMs. Statistical analyses were performed using Fisher's exact test (**c**, **e**, **i**) and empirical Bayes moderated *t* test (**h**). Source data are provided as a Source Data file.

of 28 patients (25%) exhibited high levels of serum IL36G, with the remaining patients having less than detectable sensitivity (Supplementary Fig. 9a). We note that the weight loss over the preceding 6 months (one of the three criteria for the international consensus cachexia definition[2]) in cachectic patients with high serum IL36G levels was more prominent than in those without increases in serum IL36G levels (Supplementary Fig. 9b).

To determine the effect of IL36G signaling inhibition on muscle atrophy induction in vitro, we generated CRISPR/Cas9-edited C2C12 cells lacking the expression of IL36 receptor (Fig. 5a). The knockout of

https://doi.org/10.1038/s41467-024-51873-x

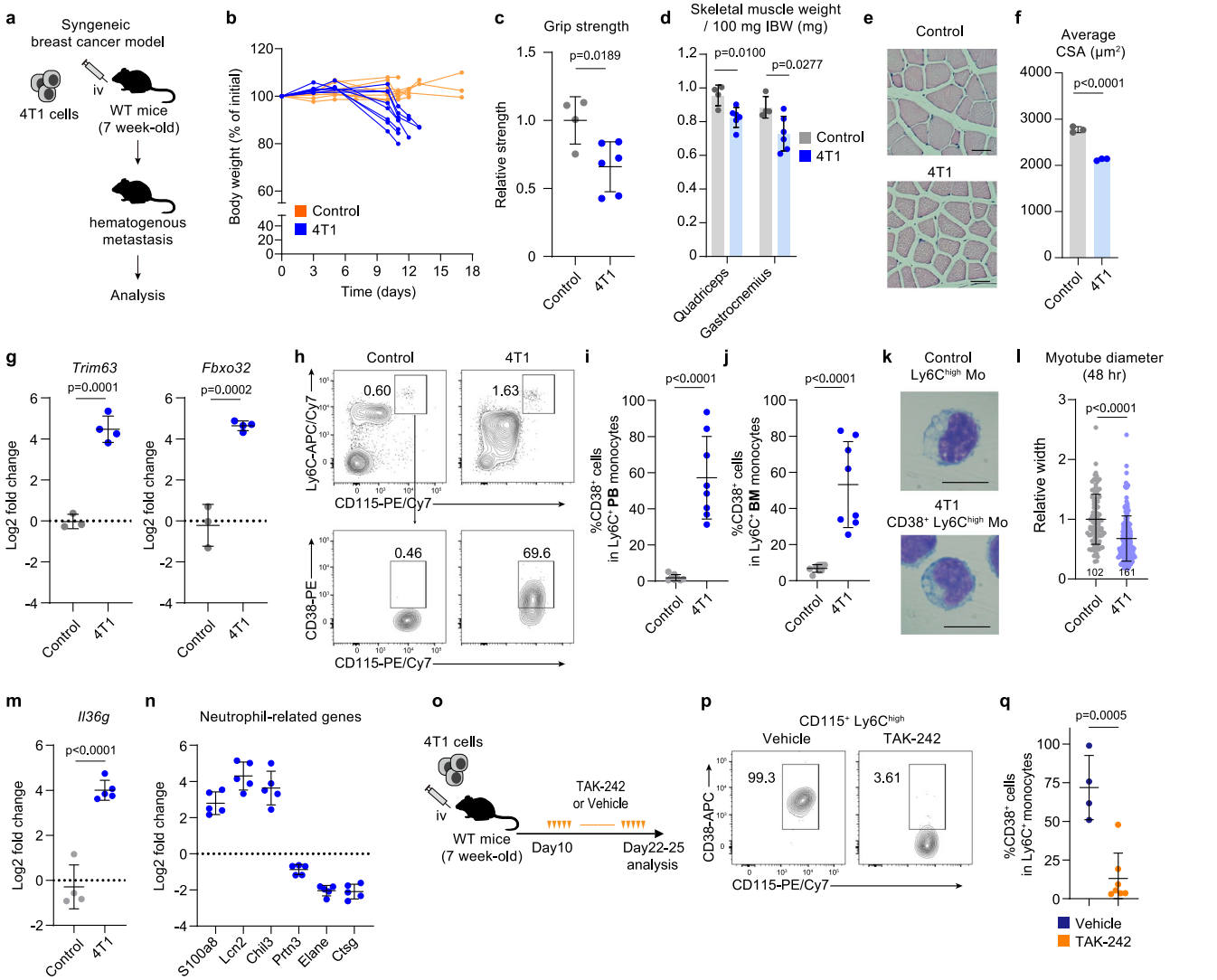

Fig. 4 | Emergence of CiMs in advanced solid cancers. a Schematic of experimental design. **b** Body weight of control and 4T1 breast cancer mice (n = 8 mice per group). **c** Forelimb grip strength of control ($n = 4$ mice) and 4T1 breast cancer ($n = 6$ mice) mice at the endpoint. The values were normalized to those of the control group. **d** Skeletal muscle weights of control ($n = 4$ mice, at day 11 to 13) and 4T1 breast cancer ($n = 6$ mice, at day 11 to 13) mice. Weights are normalized to the IBW and presented as weight/100 mg IBW. **e**, **f** HE staining and CSA of quadriceps from control and 4T1 breast cancer mice ($n = 3$ mice per group). Representative images (**e**) and average (**f**) of CSA are shown. Scale bar, 50 μm. **g** mRNA expression levels of muscle atrophy markers in quadriceps from control ($n = 3$ mice) and 4T1 breast cancer ($n = 4$ mice) mice at the endpoint. Log2 fold change values compared to mean values of control are shown. **h**, **i** Flow cytometric analysis of total PB from control and 4T1 breast cancer mice ($n = 8$ mice per group). Representative flow cytometry plots (**h**) and the frequencies of $CD38^+$ cells in PB $Ly6C^+$ inflammatory monocytes (**i**) are shown. **j** Flow cytometric analysis of the total BM from control and 4T1 breast cancer mice ($n = 8$ mice per group). The frequencies of $CD38^+$ cells in BM $Ly6C^+$ inflammatory monocytes are shown. **k** Diff-Quik staining of $CD38^+$ $Ly6C^+$ inflammatory PB monocytes from 4T1 mice with cachexia. Scale bar, 10 μm. **l** Relative diameter of C2C12 myotubes after co-culture with $Ly6C^+$ inflammatory monocytes from control mice or $CD38^+$ $Ly6C^+$ inflammatory monocytes from 4T1 breast cancer mice. Representative results from more than three independent experiments are shown. The number of muscle fibers analyzed in each sample is shown. **m** mRNA expression levels of *Il36g* in $Ly6C^+$ inflammatory monocytes from control mice ($n = 4$ mice) and in $CD38^+$ $Ly6C^+$ inflammatory monocytes from 4T1 breast cancer mice ($n = 5$ mice). Log2 fold change values compared to mean values of control are shown. **n** Expression levels of neutrophil-related genes in $Ly6C^+$ inflammatory monocytes from control mice ($n = 4$ mice) and in $CD38^+$ $Ly6C^+$ inflammatory monocytes from 4T1 breast cancer mice ($n = 5$ mice). Log2 fold change values compared to mean values of control are shown. **o** Schematic of experimental design. **p**, **q** Flow cytometric analysis of total PB from 4T1 breast cancer mice treated with vehicle ($n = 4$ mice) and TAK-242 ($n = 7$ mice). Representative flow cytometry plots (**p**) and the frequencies of $CD38^+$ cells in PB $Ly6C^+$ inflammatory monocytes (**q**) are shown. Statistical analyses were performed using a two-tailed unpaired Student's *t* test. Data are presented as the mean ± SD. Source data are provided as a Source Data file.

Il36r did not affect the viability of C2C12 cells (Supplementary Fig. 10). We then cultured *Il36r*-deficient C2C12 myotubes with $CD38^+$ $CD115^+$ $Ly6C^{high}$ inflammatory monocytes from cachectic mice with blood and solid cancers (Fig. 5b, c). Genetic inhibition of IL36G signaling significantly attenuated both CiM-mediated reduction in myotube diameter and elevation of the muscle atrophy marker (Fig. 5c and Supplementary Fig. 11). To evaluate the effect of IL36G signaling inhibition in vivo, we first integrated lentiviral transduction strategy and generated CRISPR/Cas9-edited Mo-Leukemia cells lacking the expression of Il36g (Fig. 5d). Empty vector-transduced Mo-Leukemia cells served as control. We then transplanted them into WT recipient mice (Fig. 5d). Although both groups of mice developed monocytosis, a characteristic CMML phenotype, the cachexia phenotypes in the monocytic blood cancer model, including weight loss, muscle weakness, and muscle loss, were rescued in Mo-Leukemia mice with hematopoietic cell-specific deletion of *Il36g* (Fig. 5e–g). In addition, we

https://doi.org/10.1038/s41467-024-51873-x

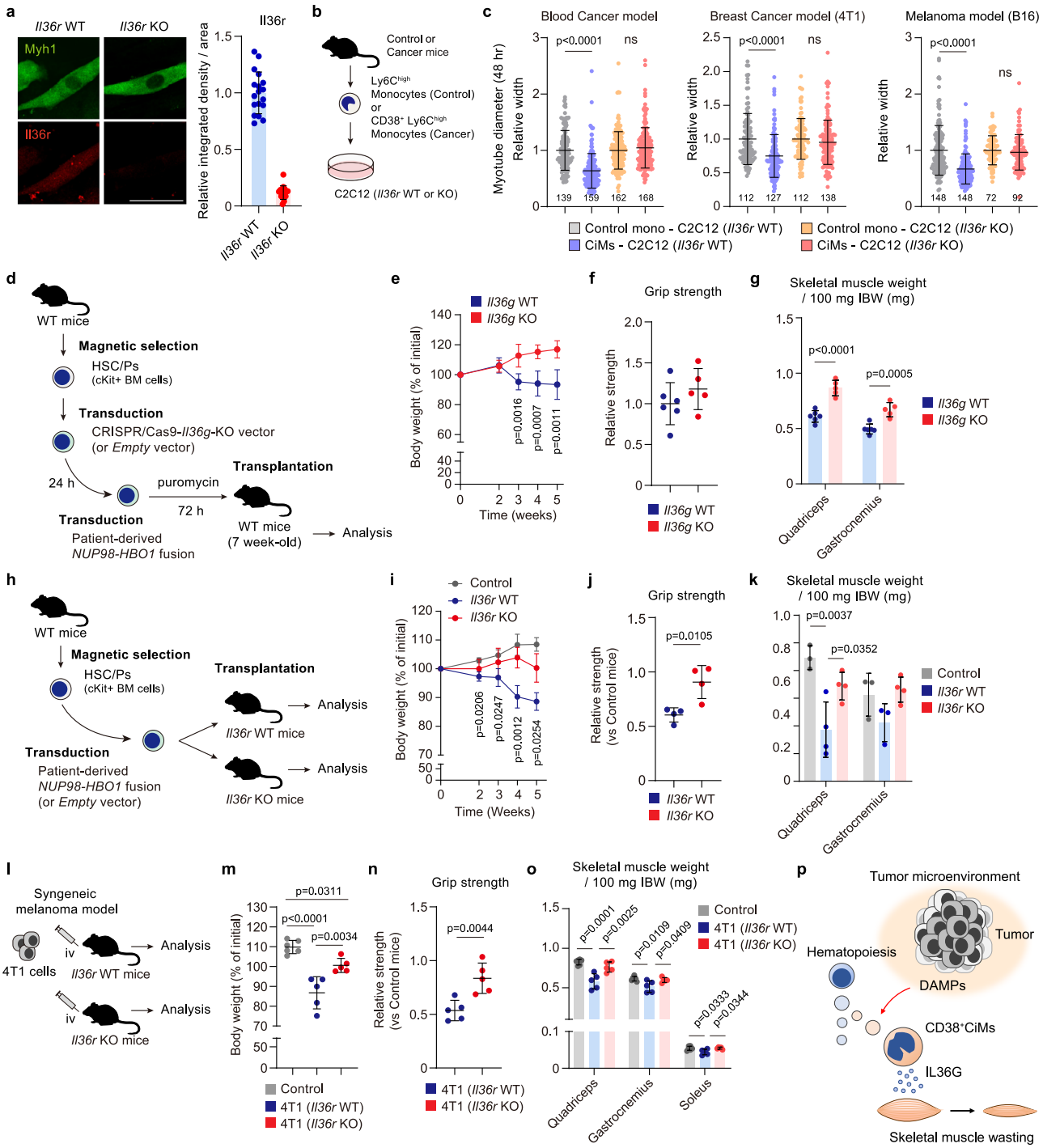

Fig. 5 | Targeting IL36G/IL1RL2 signaling in cancer cachexia. a Protein expression of Myh1 and Il36r in C2C12 myotubes with or without *Il36r*. Scale bar, 50 µm. Representative image and relative expression levels of Il36r are shown (*Il36r*-WT, $n = 18$ cells; *Il36r*-KO, $n = 15$ cells). **b** Schematic of the co-culture assay. **c** Relative diameters of C2C12 myotubes after the co-culture assay with the indicated cells. Representative results of more than three independent experiments are shown. The number of muscle fibers analyzed in each sample is shown. **d** Schematic of experimental design. **e** Body weight of *Il36g*-WT Mo-Leukemia mice ($n = 6$ mice) and *Il36g*-KO Mo-Leukemia mice ($n = 5$ mice). **f** Forelimb grip strength of *Il36g*-WT Mo-Leukemia mice ($n = 6$ mice) and *Il36g*-KO Mo-Leukemia mice ($n = 5$ mice). **g** Skeletal muscle weight of *Il36g*-WT Mo-Leukemia mice ($n = 6$ mice, at 5 weeks after BMT) and *Il36g*-KO Mo-Leukemia mice ($n = 5$ mice, at 5 weeks after BMT) at the endpoint. Weights are normalized to the IBW and presented as weight/100 mg IBW. **h** Schematic of experimental design. **i** Body weight of the control ($n = 4$ mice), Mo-Leukemia mice with *Il36r* ($n = 4$ mice), and Mo-Leukemia mice without *Il36r* ($n = 8$ mice). **j** Forelimb grip strength of Mo-Leukemia mice with or without *Il36r* ($n = 4$ mice per group) at the endpoint relative to control mice. **k** Skeletal muscle weight of control ($n = 3$ mice, at 5 weeks after BMT) and Mo-Leukemia mice with *Il36r* ($n = 4$ mice, at 3 to 5 weeks after BMT) or without *Il36r* ($n = 4$ mice, at 5 weeks after BMT). Weights are normalized to the IBW and presented as weight/100 mg IBW. **l** Schematic of experimental design. **m** Body weight of the control ($n = 6$ mice) and 4T1 breast cancer mice with or without *Il36r* ($n = 5$ mice per group). **n** Forelimb grip strength of 4T1 breast cancer mice with or without *Il36r* ($n = 5$ mice per group) at the endpoint relative to control mice. **o** Skeletal muscle weight of control ($n = 6$ mice) and 4T1 breast cancer mice with or without *Il36r* ($n = 5$ mice per group) at day 15. Weights are normalized to the IBW and presented as weight/100 mg IBW. **p** Proposed mechanism for CiM-mediated cancer cachexia development. Statistical analyses were performed using two-tailed unpaired Student's *t* test (**c**, **e**, **g**, **i**, **j**, **n**) and one-way ANOVA followed by Tukey multiple comparison test (**k**, **m**, **o**). Data are presented as the mean ± SD. NS is not significant. Source data are provided as a Source Data file.

genetically eliminated IL36 receptor expression in cachexia mice with both blood and solid cancers. Although *Il36r*-WT Mo-Leukemia mice developed progressive weight loss (Fig. 5h, i), the cachexia phenotypes in this model were attenuated in *Il36r*-deficient Mo-Leukemia mice (Fig. 5i–k). The cachexia phenotypes in the syngeneic metastatic breast cancer and melanoma models were also rescued by inhibition of IL36G signaling (Fig. 5l–o and Supplementary Fig. 12a–d). Taken together, these results suggested that the CiMs/IL36G signaling axis could be a novel therapeutic target in cancer cachexia (Fig. 5p).

Discussion

We have identified a distinct cachexia-inducible subset of inflammatory monocytes in blood and solid cancers and termed them "CiMs". CiMs exhibit a neutrophil-like gene signature and secrete IL36G, which facilitates skeletal muscle wasting and weakness. Importantly, inhibition of IL36G signaling attenuated cachexia development in mouse models of cancer cachexia, indicating that the CiMs/IL36G signaling axis is a potential therapeutic option for cancer cachexia.

Classical monocytes are differentiated from MDPs[42]. Although MDPs are thought to emerge from GMPs, recent studies have shown that MDPs emerge directly from a subset of common myeloid progenitors (CMPs), not from GMPs[30,42]. Accumulating evidence has demonstrated that GMPs can also give rise to characteristic monocytes with a neutrophil-like genetic signature[30]. We identified a distinct subset of monocytes that emerged in advanced cancer-mediated cachexia pathogenesis and found that these monocytes exhibited neutrophil-like features. Similar to the neutrophil-like monocytes, which have been described by others[30], CiMs were prominently induced upon in vivo TLR4 (but not TLR9) stimulation, and the emergence was suppressed by inhibition of TLR4, suggesting that tumor-/TME-derived TLR4 ligands are responsible for the induction of CiMs in cancer pathogenesis. Increased levels of serum damage-associated molecular patterns (DAMPs) have been reported in patients with various cancers, particularly if the cancer is at an advanced stage[43–45]. Notably, several DAMPs that have been identified in patients with advanced cancer, such as high mobility group box 1 (HMGB1) and the S100 protein family (S100A8 and S100A9), could function as TLR4 ligands[46,47]. These tumor-pathogenesis-related DAMPs are likely to promote the induction of CiMs, and thus lead to the development of cachexia in these patients.

We focused on unbiased transcriptome analysis to determine the distinct CiM-derived signaling molecules that could promote skeletal muscle atrophy and identified IL36G as a critical mediator of cachexia development. Increased expression of serum IL36G has been reported in patients with inflammatory diseases, including type-2 diabetes and obesity, autoimmune disorders, and many cancers[48,49]. IL36G is an inflammatory cytokine that belongs to the interleukin-1 (IL1) superfamily[48,49]. IL36G exhibits high-affinity binding to IL36R, recruits interleukin 1 receptor accessory protein (IL1RAP) to form the IL36 receptor complex, and activates the intracellular toll-like domain, leading to NF-κB signaling activation[48,49]. It has been well documented that the NF-κB signaling pathway can upregulate the expression of TRIM63 and FBXO32, which are master E3 ubiquitin ligases responsible for the degradation of muscle structural proteins and acceleration of muscle atrophy[1]. NF-κB signaling also impairs myoblast differentiation by suppressing *MYOD1* expression[17]. This evidence supports the critical role of the IL36G/IL36R axis in the development of cancer cachexia. Besides cancer, cachexia often occurs in patients with chronic inflammation and infection[48,49]. A protective role of IL36G against obesity has been suggested in patients with type-2 diabetes[50]. Thus, IL36G likely affects skeletal muscle homeostasis under chronic inflammation-mediated conditions or diseases.

Although neutrophil-like inflammatory monocytes have been detected in previous scRNA-Seq-based studies[30,42], their surface molecules and functional characteristics remain unclear. Our data showed that cachexia-related IL36G-producing monocytes exhibited neutrophil-like gene signatures and expressed CD38 on their cell surface. We demonstrated that $CD38^+$ inflammatory monocytes increase with cachexia progression in both blood and solid cancers, produce IL36G, and induce skeletal muscle atrophy. Thus, CD38 may be a potential surface marker for a subset of neutrophil-like monocytes. CD38 is known to function as a transmembrane enzyme that consumes both intracellular and extracellular nicotinamide adenine dinucleotide (NAD^+)[51]. Growing evidence highlights the critical role of NAD^+ levels in skeletal muscle homeostasis[52,53]. A decline in NAD^+ levels could cause skeletal muscle degeneration, whereas repletion of NAD^+ rescues skeletal muscle function. Covarrubias, et al. recently showed that the senescence-associated secretory phenotype (SASP) induces CD38 expression on myeloid innate immune cells and promotes tissue NAD^+ decline during aging[54]. Senescent cell-derived inflammatory SASP is one of the major components of the TME that can facilitate tumorigenesis, including cancer cell proliferation, invasion, epithelial-mesenchymal transition (EMT), metastasis, and immune cell reprograming[55,56]. Thus, in addition to the role of surface marker, CD38 on the surface of CiMs may also directly contribute to cachexia development via its NADase activity. However, recent advances in single-cell transcriptomics clearly demonstrate the difficulty of precisely characterizing functionally discrete cell populations using a few surface markers[29,57]. Indeed, the gene expression and protein production of Il36g in CD38-negative-inflammatory monocytes from some of the cachectic mice were also elevated compared with those in control cells. Although the majority of inflammatory monocytes from mice with prominent cachexia present CD38 on their surface and express Il36g, the Il36g-expressing inflammatory monocytes from mice at the time of weight loss onset do not always express CD38 antigen on their cell surface. These findings suggest that other surface markers, in addition to CD38, may also be expressed on the IL36G-producing CiMs.

Collectively, our data indicate that IL36G-producing neutrophil-like monocytes emerge in the context of cancer cachexia and promote skeletal muscle wasting and weakness. Our findings provide insights into the interplay between dysregulated tumor immunity and the development of cancer cachexia. Targeting the CiMs/IL36G signaling axis may be a useful therapeutic option for patients with cancer cachexia.

Methods

Ethical statement

This research complies with all relevant ethical regulations. All animal experiments were conducted in accordance with the protocols approved by the institutional animal care and use committee at the Tokyo University of Pharmacy and Life Sciences. The experiment using patients' samples was approved by the institutional ethics committee at Tokyo Metropolitan Cancer and Infectious Diseases Center, Komagome Hospital.

Mice

C57BL/6 J mice and BALB/c mice (7 to 10-week-old) were purchased from Tokyo Laboratory Animals Science (Tokyo, Japan). *Il36r* conventional knockout mice (C57BL/6 strain) were purchased from Cyagen Biosciences (Santa Clara, CA). For some experiments using 4T1 cells, *Il36r* conventional knockout mice were backcrossed more than 7 times to BALB/c mice. Mice were weighed at least twice a week. For ethical reasons, when mice developed ≥ 20% weight loss compared to the weight at the start of the experiment or tumors approached 20 mm in size (the maximal tumor size permitted by the institutional animal care and use committee), these mice were euthanized under deep anesthesia (endpoint). All animal studies were approved and conducted according to the institutional animal care protocol (L18-24, L19-10, L20-07, L21-14, L22-08, L23-04, L24-12) and guidelines of the

Tokyo University of Pharmacy and Life Sciences. All the mice were fed a standard laboratory diet (CLEA Rodent Diet CE-2, CLEA Japan) and maintained in a pathogen-free environment (23 ± 2 °C, 55 ± 5%) on an 11-h light/13-h dark cycle with food and water supplied ad libitum throughout the experimental period.

Patient samples

28 patients with both solid cancer and cachexia (esophageal cancer, $n = 6$ patients; gastric cancer, $n = 5$ patients; pancreatic cancer, $n = 4$ patients; head and neck cancers, $n = 3$ patients; lung cancer, $n = 3$ patients; melanoma, $n = 2$ patients; breast cancer, $n = 1$ patient; renal cancer, $n = 1$ patient; prostate cancer, $n = 1$ patient; ovarian cancer, $n = 1$ patient; bladder cancer, $n = 1$ patient) who were hospitalized in the palliative care unit at Tokyo Metropolitan Cancer and Infectious Diseases Center, Komagome Hospital (Tokyo, Japan) between January 2021 and October 2021 were enrolled in this study. All the patients meet the international consensus cachexia definition (either "> 5% weight loss over past 6 months" or "> 2% weight loss with body mass index (BMI) < 20"). This study was approved by the institutional ethics committee, and serum samples were isolated from the patients. All patients provided written informed consent for the use of anonymized samples and the publication of the clinical information in accordance with the Declaration of Helsinki. Detailed patients' data (sex, age, diagnosis, % weight loss over the past 6 months, BMI, and serum level of IL36G) are provided in Supplementary Data 7.

Retrovirus and lentivirus generation for mouse BMT experiments

Plat-E Packaging cells were transfected with retrovirus vectors (pMYs-IRES-eGFP, pMYs-*NUP98-HBO1*-IRES-eGFP) using FuGENE HD (Promega). The medium was changed 24 hours after transfection. The supernatant of Plat-E Packaging cells containing retroviruses was collected 48 h after transfection and concentrated using a polyethylene glycol solution. The lentiviral CRISPR-Cas9 vector containing the Cas9-coding sequence and a gRNA sequence targeting *Il36g* (pLV[CRISPR]-hCas9:T2A:Puro-U6 > mIl36g[gRNA#139]) and Scramble gRNA lentiviral control vector (pLV[CRISPR]-hCas9/Puro-U6> Scramble_gRNA1) were cloned by Vector Builder. The sequence of *Il36g*-gRNA is as follows: 5′- GGTGTGGATCTTTCGTAATC-3′. 293 T cells were transfected with these lentiviral vectors and lentiviral high-titer packaging mix (Takara/Clontech) using Lipofectamine 3000 (Thermo Fisher Scientific). The supernatant containing the retroviruses and lentiviruses was collected 48 hours after transfection and concentrated using a PEG solution.

Mouse BMT experiment

C57BL/6 J donor mice were euthanized via cervical dislocation under anesthesia. BM cells were isolated from the femurs and tibias of donor mice immediately following euthanasia. BM c-Kit$^+$ cells were then separated using an EasySep mouse cKit positive selection kit (STEMCELL Technologies). After incubation with 50 ng/mL mouse stem cell factor (SCF), mouse FMS-like tyrosine kinase 3 (FLT3) ligand (FLT3-L), mouse interleukin 6 (IL-6), and mouse thrombopoietin (TPO) (PeproTech and BioLegend) in Iscove modified Dulbecco medium (IMDM) containing 20% FBS and 1% penicillin-streptomycin, cells were transduced with the retrovirus for 60 h using RetroNectin (Takara)-coated dishes. Then, 2 to 5×10^6 of the non-sorted cells were injected through the tail vein into sublethally irradiated recipient mice. For some experiments, BM HSC/Ps isolated from donor mice were resuspended in IMDM containing 20% FBS, 50 ng/mL mouse SCF, mouse FLT3-L, mouse IL-6, and mouse TPO and immediately transduced with the lentivirus using RetroNectin-coated dishes. After 24 h of incubation, the cells were transduced with the retrovirus for 48–60 h in a RetroNectin-coated dish under puromycin treatment (3 μg/mL). The transduced and puromycin-selected cells were injected into the tail vein of sublethally irradiated WT recipient mice. *NUP98-HBO1*-BMT (Mo-Leukemia) mice before the onset of weight loss were used as "Mo-Leukemia mice without weight loss".

Solid tumor models

To generate syngeneic solid cancer, 4T1 (2.5 to 5.0×10^4 cells each) and B16 cells (2.5 to 5.0×10^4 cells each) were intravenously injected into recipient mice. BALB/c mice were used as recipients for 4T1 cells, and mice of the C57BL/6J strain were used as recipients for B16 cells.

Cell culture

C2C12 (RCB0987) and B16 cells (RCB1283) were purchased from RIKEN BRC CELL BANK. 4T1 (CRL-2539) and 293 T cells (CRL-3216) were purchased from ATCC. Plat-E cells were kindly provided by Dr. T. Kitamura. C2C12, 293 T, and Plat-E cells were maintained in Dulbecco's Modified Eagle Medium-low glucose (DMEM) containing 10% FBS and 1% penicillin-streptomycin (Fujifilm Wako Pure Chemical Corporation). 4T1 cells were maintained in RPMI1640 (Fujifilm Wako Pure Chemical Corporation) containing 10% FBS and 1% penicillin-streptomycin. B16 cells were maintained in low-glucose DMEM containing 10% FBS and 1% penicillin-streptomycin. DMEM containing 2% horse serum (Thermo Fisher Scientific) and 1% penicillin-streptomycin were used for inducing the differentiation of C2C12 cells toward myotubes.

CRISPR-Cas9 knockout of Il36r in C2C12 cells

The lentiviral CRISPR-Cas9 vector containing the Cas9-coding sequence and dual gRNA sequences targeting *Il36r* (pLV-2CRISPR-hCas9-T2A-Puro-U6>mIl1rl2-gRNA#2722-U6>mIl1rl2-gRNA#1877) were cloned by Vector Builder. The sequences of *Il36r*-gRNA are as follows: 5′-CGTCCTTTCACGTGTCATGC-3′ and 5′-TCTTGTGAACAACGTTGCTG-3′. 293 T cells were transfected with these lentivirus vectors and Lentiviral High Titer Packaging Mix (Takara/Clontech) using Lipofectamine 3000 (Thermo Fisher Scientific). The supernatant containing lentivirus was collected 48 hours following transfection and concentrated using PEG solution. C2C12 cells were then transduced with the lentivirus by spin-infection at $2000 \times g$, 32 °C for 2 h. The transduced cells were selected with puromycin (1 μg/mL).

Co-culture assay and Immunofluorescence staining

FACS-sorted murine CD115$^+$Ly6C^{high} monocytes, CD115$^+$Ly6C^{high}CD38$^+$ monocytes, CD115$^+$Ly6C^{high}CD38$^-$ monocytes, or CD115$^-$Ly6G$^+$ neutrophils (5×10^5 cells per well) were co-cultured with C2C12 myotubes for 48 h in 6 well- or 24 well-tissue culture treated plate using ThinCert transwell (0.4 μm pore size, Greiner). C2C12 cells were then fixed with 4% paraformaldehyde in PBS for 20 min, and then 15 mmol/L glycine in PBS was added. Following the treatment with 0.2% TritonX-100 in PBS, cells were washed with PBS. Following the blocking with 2% BSA in PBS, cells were stained with the following antibodies: anti- Myosin Heavy Chain (clone, MF20; catalog number, MAB4470; R&D; dilution, 5 μg/mL) and Alexa Fluor 488–conjugated anti-mouse IgG (H + L) (a21235; Invitrogen; 2 μg/mL). Cells were then washed three times with PBS, mounted with Hoechst, and examined using an Olympus FV3000-IX83 confocal fluorescence microscope (Olympus) and a BZ-X700 fluorescence microscope (Keyence). Myotube diameter was measured using ImageJ. The number of muscle fibers analyzed is indicated in each figure. Representative results from more than three independent experiments are shown in the figures.

For confirmation of Il36r knockout (KO), C2C12 cells with or without Il36r KO were fixed and stained with the following antibodies: anti- Myosin Heavy Chain (MF20; MAB4470; R&D; 5 μg/mL), anti-Il36r (ab180894; Abcam; 10 μg/mL), Alexa Fluor 488–conjugated anti-mouse IgG (H + L; a11001; Invitrogen; 2 μg/mL), and Alexa Fluor 647–conjugated anti-rabbit IgG (H + L) (a21245; Invitrogen; 2 μg/mL). Cells were then washed three times with PBS, mounted with Hoechst, and examined using an Olympus FV3000-IX83 confocal fluorescence

microscope (Olympus). The integrated density of Il36r and the area of myotube was measured using ImageJ (NIH, Bethesda, MD).

Flow cytometry

Following red blood cell lysis with Pharm Lyse (BD Biosciences), murine PB and BM cells were stained in FACS buffer (Phosphate-buffered saline (PBS) containing 2% fetal bovine serum (FBS) and 2 mM EDTA) with the following anti-mouse antibodies: CD115 (clone, AFS98; catalog number: 135524; Biolegend; dilution: 1:500), Ly6C (HK1.4; 128026, 128008; Biolegend; 1:500), Ly6G (1A8; 127612; Biolegend; 1:500), Gr1 (RB6-8C5; 108408; Biolegend; 1:500), and CD38 (90; 102708, 102712; Biolegend; 1:500). Cells were then washed with FACS buffer and resuspended in FACS buffer containing 7AAD (BioLegend). Annexin V apoptosis detection kit (Biolegend) was used to evaluate cell viability. Flow cytometric analysis was performed using FACSCanto (BD Biosciences), FACSCelesta (BD Biosciences), and CytoFLEX (Beckman Coulter). Cell sorting was performed using FACSAriaIII (BD Biosciences) or SH800 (SONY). Data were analyzed using FlowJo software (BD Biosciences, RRID:SCR_008520). Nucleated cells were gated based on forward scatter area and side scatter area (SSC-A), followed by SSC-A/side scatter height gates to exclude cell multiplets. After the morphology gates, $7AAD^+$ dead cells were excluded. Unless otherwise noted, all nucleated cells that appear following the regular gating for live singlets. Representative plots showing the sequential gating strategy for flow cytometric analysis are shown in Supplementary Fig. 13. The Gating strategy for collecting $Ly6C^{high}$ monocytes is shown in Supplementary Fig. 2.

Bulk RNA-Seq

BM cells were obtained from control mice transplanted with empty vector transduced cells and the Mo-Leukemia mice with/without weight loss. Total BM cells were immunostained, and $CD115^+$ $Ly6C^+$ cells were FACS-sorted. Total RNA was isolated using RNeasy Mini Kit (Qiagen). RNA degradation was determined on 1% agarose gel. RNA purity was determined using a NanoPhotometer spectrophotometer (IMPLEN). RNA integrity and quantitation were assessed using the RNA Nano 6000 Assay Kit and the Bioanalyzer 2100 (Agilent Technologies). RNA sequencing was performed as described before[58]. FASTQ files were processed in AltAnalyze (version 2.1.4.4)[29]. Transcript per million (TPM) estimates were calculated via a built-in call to Kallisto for read pseudoalignment and transcript quantification (Ensembl 72, mm10), and differentially expressed genes (DEGs; Log2FC > 1.0 or 0.5, $P < 0.05$) were selected in AltAnalyze (any comparison). DEGs were used as input for clustering and heatmap visualization. DEG log2 folds relative to the row mean were used in generating heatmaps and hierarchical clustering in AltAnalyze.

Single-cell RNA-Seq

FACS sorted $Ly6C^+CD115^+$ inflammatory monocytes were washed with RPMI1640 containing 10% FBS, followed by filtration with a 40 μm strainer and then resuspended in an appropriate amount of the media. Approximately 5000 cells with > 90% cell survival rate for each sample were used for GEM (Gel Bead in the emulsion) generation using Chromium Controller (10x Genomics), where RNA molecules are tagged in each cell separately. The molecular-tagged RNA fragments were converted into cDNA, followed by library establishment for next-generation sequencing using Chromium Next GEM Single Cell 3' Reagent Kits v3.1 (10x Genomics). The resulting libraries were quantified by Qubit dsDNA Assay (Thermo Fisher Scientific) and TapeStation D1000 (Agilent). The libraries were sequenced by the Illumina HiSeq platform with the following configuration: read 1: 28 bp, read 2: 91, and i7 index: 8 bp, yielding approximately 400 M paired-end reads per sample. Image analysis and base calling were conducted using software on the HiSeq instrument. Raw FASTQ reads were imported into the Cell Ranger pipeline (v3.0.2, 10x Genomics) for mapping and gene expression count analyses. The single-cell gene expression study mentioned above was conducted by Azenta Life Sciences (formerly Genewiz). Using the filtered_feature_bc_matrix, additional unsupervised ICGS was performed in the AltAnalyze pipeline (version 2.1.4.4). A moderated *t* test from AltAnalyze was used with $P < 0.05$ and Log2FC > 1.0. The minimum number of changed genes was three.

Pathway and gene cluster enrichment analysis

GO-term and pathway enrichment analyses of differentially expressed genes were performed using ToppFun in the ToppGene Suite (https://toppgene.cchmc.org/)[59]. The following parameters were used: $P < 0.05$, 15 < gene size < 500. Enrichment analysis of cluster genes was performed using GO-term-gene-set and biomarker-gene-set of the GO-Elite algorithm in AltAnalyze.

Gene set enrichment analysis (GSEA)

The data set of upregulated DEGs in CiMs was tested for enrichment in bulk RNA-Seq data sets of murine inflammatory monocytes obtained from Mo-Leukemia mice with/without weight loss, GMP- and MDP-derived inflammatory monocytes (GSE88982), inflammatory monocytes obtained from mice with breast cancer bone metastasis (GSE152795), and inflammatory monocytes obtained from patients with advanced colorectal cancer (GSE47756) and renal cell carcinoma (GSE38424) using GSEA version v4.2.3 (RRID:SCR_003199)[60]. The following parameters were used: 1000 gene_set permutations, Diff_of_Classes ranking metric and descending order real mode for gene sorting for Supplementary Fig. 4c; 1000 gene set permutations, Signal2Noise ranking metric, and descending order real mode for gene sorting for Supplementary Figs. 7c and 8a, b.

Complete blood counts

PocH-100iV Diff (Sysmex) was used for the measurement of blood cell counts.

HE staining

Quadriceps femoris muscle was fixed using a 10% formalin neutral buffer solution (Fujifilm Wako Pure Chemical Corporation) and paraffin-embedded for hematoxylin-eosin (HE). Staining was performed at Genostaff (Tokyo, Japan). Cross-sectional area (CSA) was quantified from > 200 fibers within randomly chosen fields for each mouse using ImageJ (RRID:SCR_003070).

Cytospin and Diff-Quik staining

FACS-sorted PB and BM cells were resuspended in 100 μL of 100% FBS and spun onto Matsunami SUPERFROST slides (Matsunami Glass) for 5 min at 500 rpm using a Cyto-Tek 2500 cytocentrifuge (Sakura Finetek). Slides of mice PB and BM cells were then fixed and stained using Diff-Quik (Sysmex).

Grip strength test

Forelimb grip strength was measured using the MK-380Si grip strength meter (Muromachi Kikai). Mice were placed on a metal mesh and allowed to grip it with forelimbs. The tail was horizontally pulled backward. The peak tension was recorded at the time the mice released the mesh. Measurement was repeated ten times and the mean was calculated.

Quantitative RT-PCR

The total RNA of hematopoietic cells and C2C12 cells was isolated using RNeasy Mini or Micro kit (Qiagen) and reverse transcribed to cDNA using RevertraAce (Toyobo). C2C12 cells for Quantitative RT-PCR were collected 24 h after the start of the co-culture assay. Murine skeletal muscle was homogenized using Biomasher III (Nippi) for RNA extraction. The total RNA of muscle tissue was isolated using RNeasy Fibrous Tissue Mini Kit (Qiagen) and reverse transcribed to cDNA using

RevertraAce (Toyobo). Quantitative PCR was performed using Applied Biosystems Step One Plus thermal cycler (Applied Biosystems), Power SYBR Green PCR master mix (Applied Biosystems), and the following primers: for mouse *Il36g*, 5′-AGAGTAACCCCAGTCAGCGTG-3′ and 5′-AGGGTGGTGGTACAAATCCAA-3′; for mouse *Trim63*, 5′-GTGTGAGGTGCCTACTTGCTC-3′ and 5′-GCTCAGTCTTCTGTCCTTGGA-3′; for mouse *Fbxo32*, 5′-CAGCTTCGTGAGCGACCTC-3′ and 5′-GGCAGTCGAGCCGTCCAGTC-3′; for mouse *Lcn2*, 5′-CTGAATGGGTGGTGAGTGTG-3′ and 5′-GCTCTCTGGCAACAGGAAAG-3′; for mouse *S100a8*, 5′-CCTTTGTCAGCTCCGTCTTC-3′ and 5′-TAGAGGGCATGGTGATTTCC-3′; for mouse *Chil3*, 5′-GAAGGAGCCACTGAGGTCTG-3′ and 5′-CACGGCACCTCCTAAATTGT-3′; for mouse *Elane*, 5′-ACTCTGGCTGCCATGCTACT-3′ and 5′-GCCACCAACAATCTCTGAGG-3′; for mouse *Ctsg*, 5′-CAACGGTTCTGGAAAGATGC-3′ and 5′-CTTCTCGGCCTCCAATGAT-3′; for mouse *Prtn3*, 5′-AGCTACCCATCCCCCAAG-3′ and 5′-TCGTGCCCACCTACAATCTT-3′; for mouse *Actb*, 5′-ACACCCGCCACCAGTTC-3′ and 5′-TACAGCCCGGGGAGCAT-3′; and for mouse *Hprt*, 5′-TTGTATACCTAATCATTATGCCGAG-3′ and 5′-CATCTCGAGCAAGTCTTTCA-3′.

Administration of LPS and unmethylated CpG DNA

LPS (L6529, Sigma; 2 μg/mouse) was injected intraperitoneally once every other day for a total of 2 injections. CpG oligonucleotide (D35, CN-65001, GeneDesign; 12 μg/mouse) was injected intraperitoneally once every other day up to 14 times. Mice were analyzed 24 hours after final administration.

TAK-242 Treatment

From day 10 after tumor cell injection, B16 and 4T1 metastasis models were treated with 3 mg/kg TAK-242 (S7455, Selleck) or DMSO vehicle intraperitoneally daily up to 15 times.

ELISA

FACS-sorted 1×10^5 indicated cells were seeded on a 96-well flat bottom plate and incubated in 100 µL RPMI1640 for 24 h. The culture medium was then immediately snap-frozen in liquid nitrogen and stored at − 80 °C until usage. Il36g concentrations were measured using a Mouse Interleukin-36 gamma ELISA Kit (MyBioSource) according to the manufacturer's instructions. Absorbance was measured at 450 nm using EnSpire (Perkin Elmer). For serum from patients with cachexia, IL36G concentrations were measured using a Human IL36G ELISA kit (Invitrogen). SpectraMax ABS (Molecular Device) was used for the measurement of absorbance at 450 nm.

Statistics and reproducibility

GraphPad Prism (v8) (GraphPad, RRID:SCR_002798) was used. Statistical analyses for the comparison of two independent, normally distributed samples were compared using the two-tailed Student's *t* test. For multiple pairwise comparisons, the data were analyzed by one-way ANOVA followed by the Tukey multiple comparison test. For pathway or GO-term enrichment analysis, Fisher's exact test was used. An empirical Bayes moderated *t*-test was used for the identification of differentially expressed genes in AltAnalyze. Statistical significance was set at $P < 0.05$. No statistical method was used to predetermine the sample size. No data were excluded from the analyses. The experiments were not randomized. The Investigators were not blinded to allocation during experiments and outcome assessment.

Reporting summary

Further information on research design is available in the Nature Portfolio Reporting Summary linked to this article.

Data availability

The Bulk-RNA-Seq and scRNA-Seq data reported in this paper have been deposited in Gene Expression Omnibus (GEO, RRID:SCR_005012) as GEO SuperSeries GSE210003. The public datasets reused in this paper are available in the GEO database under accession codes; GSE88982, GSE152795, GSE47756, and GSE38424. The raw and processed data generated in this study are provided in the Supplementary Information/Source Data file. Source data are provided in this paper.

References

1. Argilés, J. M., Busquets, S., Stemmler, B. & López-Soriano, F. J. Cancer cachexia: understanding the molecular basis. *Nat. Rev. Cancer* **14**, 754–762 (2014).
2. Fearon, K. et al. Definition and classification of cancer cachexia: an international consensus. *Lancet Oncol.* **12**, 489–495 (2011).
3. von Haehling, S. & Anker, S. D. Cachexia as a major underestimated and unmet medical need: facts and numbers. *J. Cachexia Sarcopenia Muscle* **1**, 1–5 (2010).
4. Balkwill, F., Charles, K. A. & Mantovani, A. Smoldering and polarized inflammation in the initiation and promotion of malignant disease. *Cancer Cell* **7**, 211–217 (2005).
5. Schreiber, R. D., Old, L. J. & Smyth, M. J. Cancer immunoediting: integrating immunity's roles in cancer suppression and promotion. *Science* **331**, 1565–1570 (2011).
6. Bruni, D., Angell, H. K. & Galon, J. The immune contexture and Immunoscore in cancer prognosis and therapeutic efficacy. *Nat. Reviews Cancer* **20**, 662–680 (2020).
7. Gabrilovich, D. I., Ostrand-Rosenberg, S. & Bronte, V. Coordinated regulation of myeloid cells by tumours. *Nat. Rev. Immunol.* **12**, 253–268 (2012).
8. Galdiero, M. R., Varricchi, G., Loffredo, S., Mantovani, A. & Marone, G. Roles of neutrophils in cancer growth and progression. *J. Leukocyte Biol.***103**, 457–464 (2018).
9. Oberg, H. H., Wesch, D., Kalyan, S. & Kabelitz, D. Regulatory interactions between neutrophils, tumor cells and T cells. *Front. Immunol.* **10**, 1690 (2019).
10. Maier, B. et al. A conserved dendritic-cell regulatory program limits antitumour immunity. *Nature* **580**, 257–262 (2020).
11. Molgora, M. et al. TREM2 Modulation remodels the tumor myeloid landscape enhancing Anti-PD-1 immunotherapy. *Cell* **182**, 886–900.e817 (2020).
12. Zhang, Q. et al. Landscape and dynamics of single immune cells in hepatocellular carcinoma. *Cell* **179**, 829–845 (2019).
13. Zilionis, R. et al. Single-cell transcriptomics of human and mouse lung cancers reveals conserved myeloid populations across individuals and species. *Immunity* **50**, 1317–1334 (2019).
14. Mantovani, A., Marchesi, F., Malesci, A., Laghi, L. & Allavena, P. Tumour-associated macrophages as treatment targets in oncology. *Nat. Rev. Clin. Oncol.* **14**, 399–416 (2017).
15. Hanna, R. N. et al. Patrolling monocytes control tumor metastasis to the lung. *Science* **350**, 985–990 (2015).
16. Cassetta, L. et al. Human tumor-associated macrophage and monocyte transcriptional landscapes reveal cancer-specific reprogramming, biomarkers, and therapeutic targets. *Cancer Cell* **35**, 588–602.e510 (2019).
17. Baazim, H., Antonio-Herrera, L. & Bergthaler, A. The interplay of immunology and cachexia in infection and cancer. *Nat. Rev. Immunol.* **22**, 309–321 (2022).
18. Fajgenbaum, D. C. & June, C. H. Cytokine storm. *N. Engl. J. Med.* **383**, 2255–2273 (2020).
19. Talbert, E. E. et al. Circulating monocyte chemoattractant protein-1 (MCP-1) is associated with cachexia in treatment-naïve pancreatic cancer patients. *J. Cachexia Sarcopenia Muscle* **9**, 358–368 (2018).
20. Petruzzelli, M. et al. Early neutrophilia marked by aerobic glycolysis sustains host metabolism and delays cancer cachexia. *Cancers* **14**, 963 (2022).

21. Olson, B. et al. Lipocalin 2 mediates appetite suppression during pancreatic cancer cachexia. *Nat. Commun.* **12**, 2057 (2021).
22. Tadmor, T. et al. Monocyte count at diagnosis is a prognostic parameter in diffuse large B-cell lymphoma: results from a large multicenter study involving 1191 patients in the pre- and post-rituximab era. *Haematologica* **99**, 125–130 (2014).
23. Feng, F. et al. Low lymphocyte count and high monocyte count predicts poor prognosis of gastric cancer. *BMC Gastroenterol.* **18**, 148 (2018).
24. Sanford, D. E. et al. Inflammatory monocyte mobilization decreases patient survival in pancreatic cancer: a role for targeting the CCL2/CCR2 axis. *Clin. Cancer Res.* **19**, 3404–3415 (2013).
25. Shigeta, K. et al. High absolute monocyte count predicts poor clinical outcome in patients with castration-resistant prostate cancer treated with docetaxel chemotherapy. *Ann. Surg. Oncol.* **23**, 4115–4122 (2016).
26. Selimoglu-Buet, D. et al. Characteristic repartition of monocyte subsets as a diagnostic signature of chronic myelomonocytic leukemia. *Blood* **125**, 3618–3626 (2015).
27. Patnaik, M. M. & Tefferi, A. Chronic Myelomonocytic leukemia: 2020 update on diagnosis, risk stratification and management. *Am. J. Hematol.* **95**, 97–115 (2020).
28. Hayashi, Y. et al. NUP98-HBO1-fusion generates phenotypically and genetically relevant chronic myelomonocytic leukemia pathogenesis. *Blood Adv.* **3**, 1047–1060 (2019).
29. Olsson, A. et al. Single-cell analysis of mixed-lineage states leading to a binary cell fate choice. *Nature* **537**, 698–702 (2016).
30. Yáñez, A. et al. Granulocyte-monocyte progenitors and monocyte-dendritic cell progenitors independently produce functionally distinct monocytes. *Immunity* **47**, 890–902.e894 (2017).
31. Poltorak, A. et al. Defective LPS signaling in C3H/HeJ and C57BL/10ScCr mice: mutations in Tlr4 gene. *Science* **282**, 2085–2088 (1998).
32. Park, B. S. et al. The structural basis of lipopolysaccharide recognition by the TLR4-MD-2 complex. *Nature* **458**, 1191–1195 (2009).
33. Wang, G. et al. Metastatic cancers promote cachexia through ZIP14 upregulation in skeletal muscle. *Nat. Med.* **24**, 770–781 (2018).
34. Petruzzelli, M. et al. A switch from white to brown fat increases energy expenditure in cancer-associated cachexia. *Cell Metab.* **20**, 433–447 (2014).
35. Das, S. K. et al. Adipose triglyceride lipase contributes to cancer-associated cachexia. *Science* **333**, 233–238 (2011).
36. Hu, Y. et al. Cancer-cell-secreted miR-204-5p induces leptin signalling pathway in white adipose tissue to promote cancer-associated cachexia. *Nat. Commun.* **14**, 5179 (2023).
37. Segatto, M. et al. Epigenetic targeting of bromodomain protein BRD4 counteracts cancer cachexia and prolongs survival. *Nat. Commun.* **8**, 1707 (2017).
38. Takashima, K. et al. Analysis of binding site for the novel small-molecule TLR4 signal transduction inhibitor TAK-242 and its therapeutic effect on mouse sepsis model. *Br. J. Pharmacol.* **157**, 1250–1262 (2009).
39. Ma, R. Y. et al. Monocyte-derived macrophages promote breast cancer bone metastasis outgrowth. *J. Exp. Med.* **217**, e20191820 (2020).
40. Hamm, A. et al. Tumour-educated circulating monocytes are powerful candidate biomarkers for diagnosis and disease follow-up of colorectal cancer. *Gut* **65**, 990–1000 (2016).
41. Chittezhath, M. et al. Molecular profiling reveals a tumor-promoting phenotype of monocytes and macrophages in human cancer progression. *Immunity* **41**, 815–829 (2014).
42. Guilliams, M., Mildner, A. & Yona, S. Developmental and functional heterogeneity of monocytes. *Immunity* **49**, 595–613 (2018).
43. Chung, H. W. et al. Serum high mobility group box-1 (HMGB1) is closely associated with the clinical and pathologic features of gastric cancer. *J. Transl. Med.* **7**, 38 (2009).
44. Krysko, D. V. et al. Immunogenic cell death and DAMPs in cancer therapy. *Nat. Rev. Cancer* **12**, 860–875 (2012).
45. Hernandez, C., Huebener, P. & Schwabe, R. F. Damage-associated molecular patterns in cancer: a double-edged sword. *Oncogene* **35**, 5931–5941 (2016).
46. Yu, M. et al. HMGB1 signals through toll-like receptor (TLR) 4 and TLR2. *Shock* **26**, 174–179 (2006).
47. Vogl, T. et al. Mrp8 and Mrp14 are endogenous activators of Toll-like receptor 4, promoting lethal, endotoxin-induced shock. *Nat. Med.* **13**, 1042–1049 (2007).
48. Queen, D., Ediriweera, C. & Liu, L. Function and regulation of IL-36 signaling in inflammatory diseases and cancer development. *Front. Dev. Biol.* **7**, 317 (2019).
49. Elias, M. et al. IL-36 in chronic inflammation and fibrosis - bridging the gap? *J. Clin. Invest.* **131**, e144336 (2021).
50. Giannoudaki, E. et al. Interleukin-36 cytokines alter the intestinal microbiome and can protect against obesity and metabolic dysfunction. *Nat. Commun.* **10**, 4003 (2019).
51. Chini CCS et al. CD38 ecto-enzyme in immune cells is induced during aging and regulates NAD(+) and NMN levels. *Nat. Metab.* **2**, 1284–1304 (2020).
52. Frederick, D. W. et al. Loss of NAD homeostasis leads to progressive and reversible degeneration of skeletal muscle. *Cell Metab.* **24**, 269–282 (2016).
53. Ryu, D. et al. NAD+ repletion improves muscle function in muscular dystrophy and counters global PARylation. *Sci. Transl. Med.* **8**, 361ra139 (2016).
54. Covarrubias, A. J. et al. Senescent cells promote tissue NAD(+) decline during ageing via the activation of CD38(+) macrophages. *Nat. Metab.* **2**, 1265–1283 (2020).
55. Coppé, J. P., Desprez, P. Y., Krtolica, A. & Campisi, J. The senescence-associated secretory phenotype: the dark side of tumor suppression. *Annu. Rev. Pathol.* **5**, 99–118 (2010).
56. Hanahan, D. Hallmarks of cancer: New dimensions. *Cancer Discov.* **12**, 31–46 (2022).
57. Paul, F. et al. Transcriptional heterogeneity and lineage commitment in myeloid progenitors. *Cell* **163**, 1663–1677 (2015).
58. Aoyagi, Y. et al. Mitochondrial fragmentation triggers ineffective hematopoiesis in myelodysplastic syndromes. *Cancer Discov.* **12**, 250–269 (2022).
59. Chen, J., Xu, H., Aronow, B. J. & Jegga, A. G. Improved human disease candidate gene prioritization using mouse phenotype. *BMC Bioinformatics* **8**, 392 (2007).
60. Subramanian, A. et al. Gene set enrichment analysis: a knowledge-based approach for interpreting genome-wide expression profiles. *Proc. Natl. Acad. Sci. USA* **102**, 15545–15550 (2005).

Acknowledgements

We thank Dr. Keiko Tanaka (Department of Palliative Care, Tokyo Metropolitan Cancer and Infectious Disease Center Komagome Hospital, Tokyo, Japan) for serum samples from patients. This study was supported by the JSPS KAKENHI Grant Number 22K19462 (H.H).

Author contributions

Conceptualization: Y. Hayashi., H.H. Methodology: Y. Hayashi. Investigation: Y. Hayashi., Y.K.A., S.N., N.M., R.N., R.I., A.I., Y.W., K.Y., H.K., and Y. Harada. Writing – original draft: Y. Hayashi.

Competing interests

H.H. reports consultancy for Novartis. The remaining authors declare no competing interests.

Additional information

Supplementary information The online version contains supplementary material available at https://doi.org/10.1038/s41467-024-51873-x.

Correspondence and requests for materials should be addressed to Yoshihiro Hayashi or Hironori Harada.

Peer review information *Nature Communications* thanks the anonymous reviewers for their contribution to the peer review of this work. A peer review file is available.